Strain engineering the atomic and electronic structure of graphene at the nanometer scale

– Final report –

Till the end of the project 10 publications have appeared, with a total impact factor of 99.5. These publications have already attracted about 400 independent citations. Several other results are under various stages of publication: from submitting the revised version to preparing the manuscript. The main results of the present project can be classified into four main areas, in accordance with the original proposal:

1) The fabrication and study of strain induced graphene superlattices
2) Strain engineering of graphene by AFM lithography and thermal cycling
3) Correlated electronic states in graphene
4) Strain engineering and superlattices of other 2D materials

In the following we will present in more details the results of each of the above mentioned areas, also mentioning the corresponding publications where further details can be found..

The fabrication and study of graphene superlattices

The fabrication of 1D superlattices on suspended graphene membranes have been demonstrated by us before the start of the project. Within this project we mainly studied the formation and properties of 2D superlattices of graphene supported by crystalline surfaces. In this case the mechanical strain is primarily introduced into the graphene by the mismatch of the lattice constants of graphene and the supporting surface. The van der Waals interaction tries to drive the system into full registry. However, this introduces mechanical strain, primarily in the single atom thick graphene layer. To locally become into register with the substrate, the graphene lattice relaxes the emerging mechanical strain through out-of-plane deformation, giving rise to a periodic nanoscale modulation of its atomic structure (graphene superlattice). Besides lattice mismatch the periodicity of such moiré graphene superlattice can also be tuned by the rotation angle between the graphene and the substrate.

Graphene on Cu 111

*P. Süle, M. Szendrő, C. Hwang, L. Tapasztó: Carbon **77,** 1082-1087 (2014)*

Within the project we first studied the 2D moiré superlattices of graphene emerging on Cu 111 substrates by scanning tunneling microscopy and molecular dynamics simulations.

Graphene on copper is a system of high technological relevance, as Cu is one of the most widely used substrates for the growth of graphene. Scanning tunneling microscopy is one of the most suitable characterization tools for studying graphene superlattices. This is mainly due to the atomic resolution capability of the STM and its ability to reliably detect extremely small height variations. Our STM measurements have been performed at low temperatures (78 K) and under UHV conditions. We have shown that a new rotated phase can exist on Cu (111) with so far the smallest periodicity of 1.5 nm and the largest rotation angle of 10.4 degree.
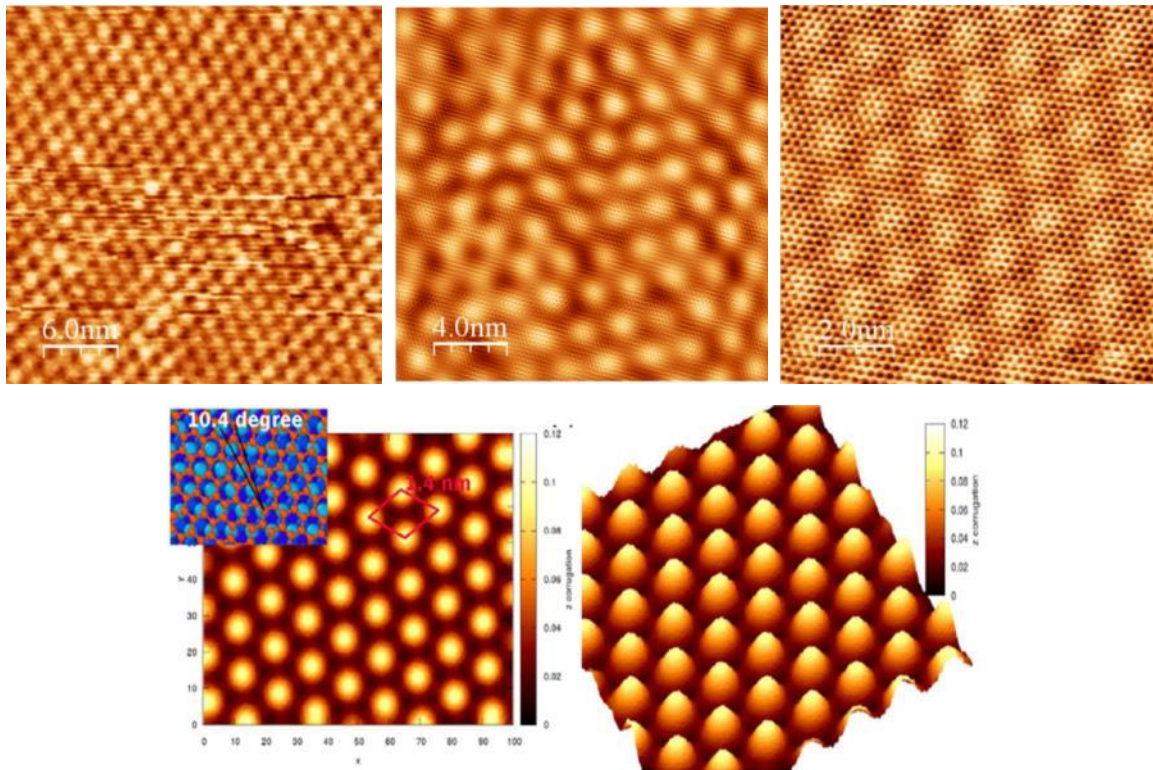
Fig. 1 *Atomic resolution STM images of various graphene superlattices on Cu(111). Molecular dynamics simulations of the novel graphene superlattice of 10.4 degrees rotation angle (bottom row.*

Experimental (STM) and theoretical classical molecular dynamics (CMD) methods have been employed to characterize the new rotated phase. We have developed a new interfacial force field to describe various graphene superlattices emerging on Cu (111) substrate. No such interface interaction potential, adequately describing the superlattices of graphene/Cu (111) interface has been available so far. Using classical molecular dynamics simulations we have shown that our method can provide reasonably accurate structural results even for weakly bound (low-corrugated) extended systems such as graphene on copper. We also reported the experimental observation of a new rotated phase of 1.5nm periodicity that has not been previously observed experimentally. Using the new potential we have successfully reproduced the observed novel phase for rotation angle of 10.5 degree, including the fine structure of the

superlattice, without any further parameter adjustment. Furthermore, our model predicts the existence of various superlattices. We found that, while aligned and low-angle rotated structures display a clearly detectable corrugation, further increasing the misalignment quickly flattens the graphene sheet. Angles larger than 15 degree are predicted to yield ultra-flat graphene on Cu 111.

Graphene on Au (111)

We have performed Scanning Tunneling Microscopy (STM) measurements under ambient conditions on graphene samples grown by CVD on polycrystalline Cu foils and transferred onto gold substrates with large atomically flat Au 111 terraces by using the standard PMMA assisted transfer technique. The parallel stripes with bending angles of about 120 degrees running across the STM image in Fig. 2a are due to the well-known herringbone reconstruction of the Au 111 surface. The periodic honeycomb lattice visible in the STM image is not the atomic graphene lattice (0.246 nm), but a moiré superlattice of much larger (1.1 nm) periodicity. While most of the surface is covered by a hexagonal lattice of depressions, upon closer examination in several triangular areas of the herringbone junctions (marked by white circles) the graphene superlattice morphology changes to protrusions of the same periodicity, as evidenced in Fig. 2b.
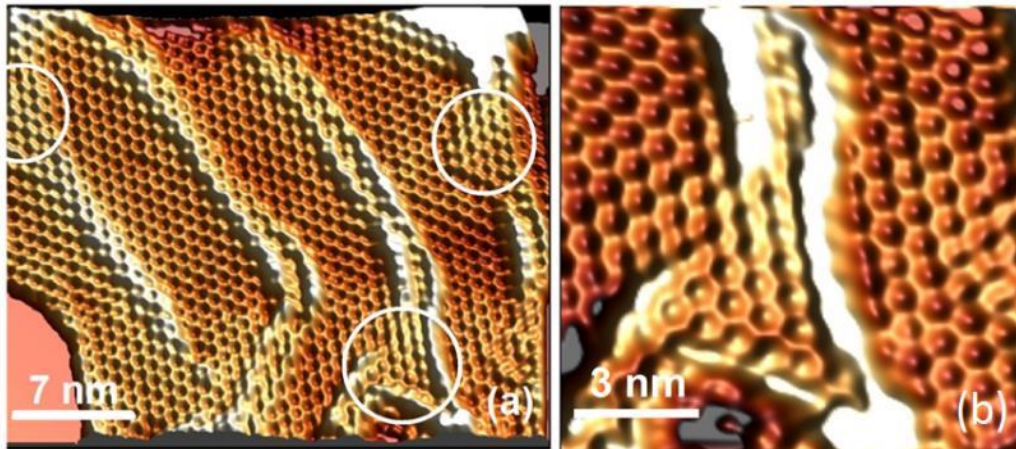
Fig 2: *a) 3D STM image of graphene on herringbone reconstructed Au(111) surface revealing a nanomesh type hexagonal graphene superlattice of 1.1 nm periodicity as well as the more common protrusion superlattice in the areas marked by white circles. b) Higher magnification STM image evidencing the coexistence of the convex (periodic protrusions within the triangular herringbone junction) and concave (periodic depressions) superlattice morphologies*

High resolution STM images displaying both the atomic lattice of graphene and the superlattice have also been acquired as shown in Fig. 3a. A honeycomb lattice is apparent for both the atomic lattice and superlattice. From atomic resolution images one can experimentally determine the rotation angle between the graphene atomic lattice and the moiré superlattice, which was measured to be 12 +/- 1 degree.
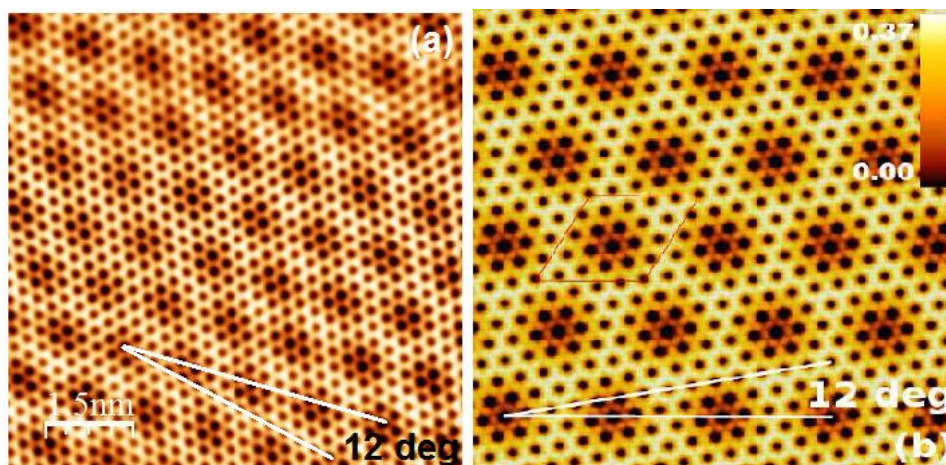
Fig 3. *a) Atomic resolution STM image of the graphene nanomesh on Au 111, displaying a hexagonal superlattice of 1.1 nm (+/- 0.1 nm) periodicity, 0.3 Å (+/- 0.1 Å) corrugation, and 12° (+/- 1°) rotation angle. b) Simulated STM image of the graphene superlattice emerging on Au(111) obtained by DFT calculations confirming the experimentally observed nanomesh morphology with a remarkable quantitative agreement (1.1 nm, 0.3 Å, 12°).*

DFT calculations show that both concave and convex graphene morphologies are stable but the nanomesh geometry was found to be of lower energy on Au (111) in agreement with our experimental results. The energy of the concave (nanomesh) and convex configurations (per carbon atom) as calculated to be -7.340 eV, and -7.332 eV, respectively. Therefore, we find that the concave (nanomesh) topography is slightly more stable than the convex one, although the energy difference is within the range of thermal energy at room temperature. The coexistence of the two morphologies can be explained due to this small energy difference, while the dominant nature of the nanomesh morphology might be related to the reconstruction of the Au(111) substrate further stabilizing the nanomesh (concave) morphology. Convex protrusion superlattice observed in the small triangular areas defined by the herringbone junctions of the Au(111) substrate most probably emerge due to the subtle changes in the local gold surface structure, altering the overlayer/substrate interaction.

The observation and stability of the nanomesh morphology so far elusive in graphene on metallic substrates can be related to the reconstruction of the Au(111) surface in the presence of graphene revealed by both DFT and molecular dynamics simulations. The fact that both convex and concave graphene superlattice morphologies are stable under similar conditions can open the way towards reversibly tuning their geometry between the two complementary landscapes that in turn can be exploited to control the adsorption and guide the assembly of various molecules on graphene.

Strain engineering of graphene by AFM lithography and thermal cycling

Strain patterning by Atomic Force Microscopy

P. Nemes-Incze, G. Kukucska, J. Koltai, J. Kürti, C. Hwang, L. Tapasztó, L. P Biró

We have developed a nanofabrication technique by which custom strain patterns can be defined with a precision of order of 10 nm and well defined crystallographic orientation in supported graphene sheets. We applied AFM indentation which deforms (strains) graphene elastically while the SiO_2 substrate undergoes a plastic deformation. The process leaves graphene pinned to the grooves formed in the substrate. During indentation, the AFM tip is lowered towards the sample surface until a pre-set cantilever deflection. After the point like indentation the tip is either lifted creating a single dot or it is moved along a straight line creating an indentation line. The procedure can be repeated with changing the tip location, yielding a periodic indentation dot or line lattice as illustrated in Fig. 4. For the indentation experiments a diamond-like carbon coated silicon AFM probe is used, with a nominal force constant and a tip radius of 40 N/m and 15 nm respectively. The crystallographic directions of the graphene can be revealed before patterning, by imaging the surface using a softer cantilever. In this case the frictional forces experienced by the tip are modulated by the atomic lattice (see Fig. 4). No significant damage to the graphene has been observed either through AFM or Raman measurements up to an indentation depth of 1.5 nm.
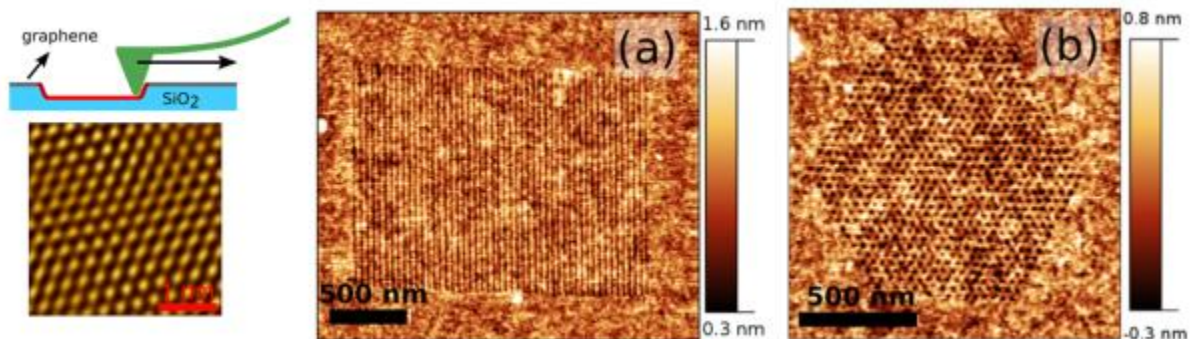
Fig. 4. *Schematics of the AFM indentation process. Strain patterns of linear 1D grating (a) and a 2D dot lattice of hexagonal symmetry (b) have been created in graphene layers on top of Si/SiO₂ substrate.*

The magnitude of strain induced in these structures can be tuned by the depth of the indentation. In Fig. 5 we show different linear strain lattices with 50 nm periodicity and increasing indentation depth. Above 1.5 nm indentation depth the rupture of the graphene sheet becomes more frequent.
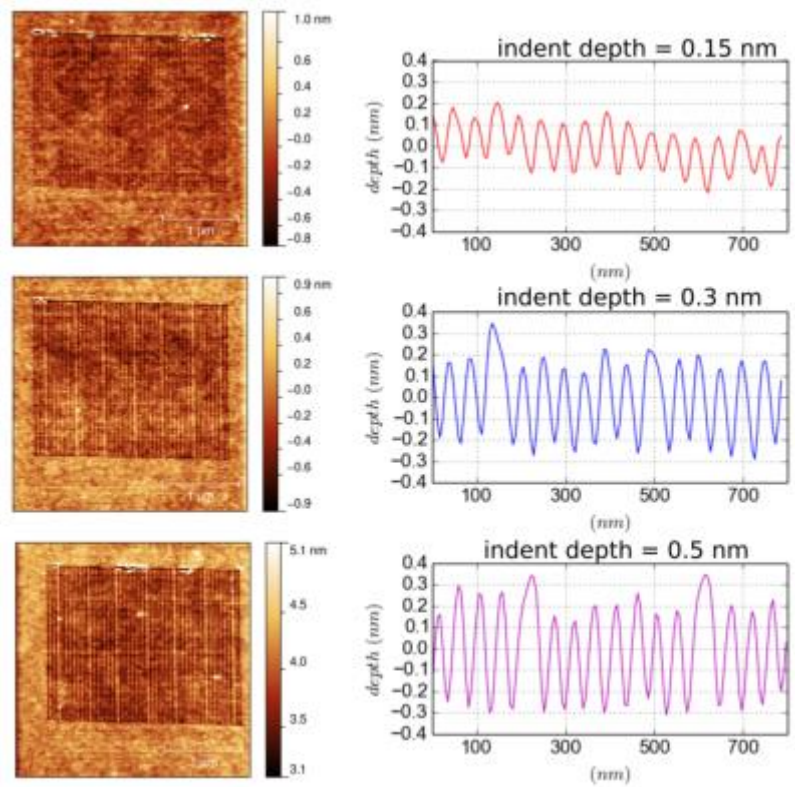
Fig. 5. *Tuning the magnitude of the strain. AFM topography images (left column) and height sections (right column) of the line patterns for different indentation depths.*

For electronic device applications the strain can interact with the charge carriers by scattering them as well as through the pseudo-magnetic field it induces. Ideally a strain pattern could create a quasi-uniform pseudo-magnetic field, which in turn can give rise to Landau levels in the band structure similar to the one induced by real external magnetic fields. However, the pseudo-magnetic fields emerging due to strain can be much higher up to several thousands of Tesla, as well as they are "built-in", not requiring externally applied magnetic fields, which is a huge advantage for device applications. To understand the behavior of the electronic devices based on such strain-engineered graphene samples with nanoscale strain patterns we need to know the pseudo-magnetic field distribution within the samples. Therefore we have performed detailed calculations based on the experimental data on the morphology of the patterned graphene sheets. For a hexagonal do array the results of such an analysis are displayed in Fig. 6.
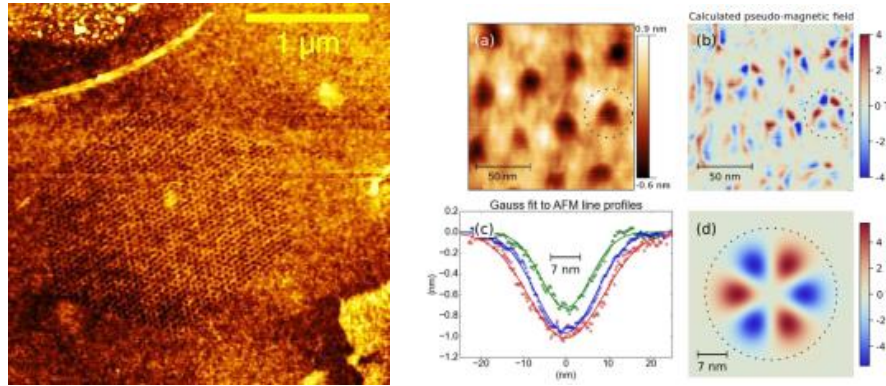
Fig. 6. *AFM image of a hexagonal indentation dot lattice, and the corresponding analysis of the strain and pseudo/magnetic field it induces. The resulting pseudo-magnetic field is calculated based on the experimental indentation profiles.*

Using the above described AFM nano-indentation technique we have prepared several strain patterned graphene samples on Si/SiO₂ substrates with predefined marker systems, that subsequently have been integrated into electronic devices. Both samples with linear and dot array have been prepared. Some of the prepared samples and devices are displayed below:
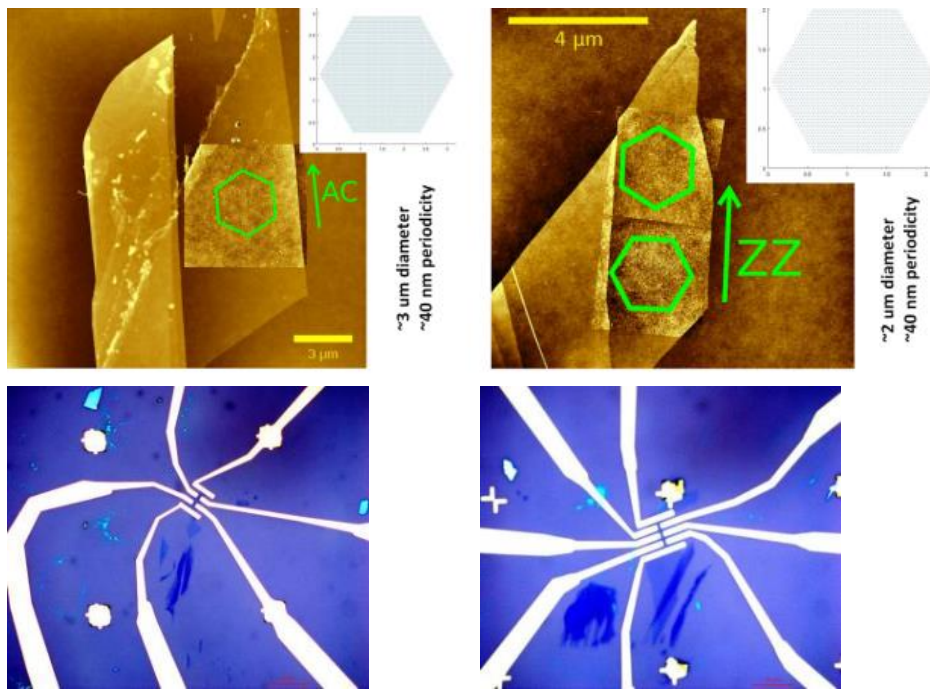
Fig. 7. *AFM images of graphene flakes with large area indentation dot lattices of hexagonal symmetry marked by green hexagons (top row). The insets of the AFM images show the plans of the dot pattern each containing several thousand of indentation dots. Optical microscopy images of various electronic devices based on strain-engineered graphene samples.*

Transport measurements have been performed on such strain patterned graphene samples, at low temperatures and in high magnetic field. The interpretation of the results is not yet conclusive, more experiments are underway..

Ultra-corrugated graphene and surface enhanced Raman scattering

-    *manuscript under preparation -*

Until now the strain patterns introduced by us into the graphene were periodic. Another approach to induce mechanical strain in graphene is to exploit the thermal expansion coefficient difference between the substrate and graphene. As graphene has a negative thermal expansion coefficient huge strains can be induced in its structure through annealing it on various substrates. We have developed a technique based on cyclic annealing of graphene on SiO_2/Si substrate that gives rise to ultra-corrugated graphene sheets as evidenced by STM images in Fig. 8. By tunneling spectroscopy measurements and DFT calculations we have shown that the electronic structure of graphene changes above a critical corrugation level, above which charge carriers can be confined within the nanoscale graphene wrinkles (Fig. 8, 9).
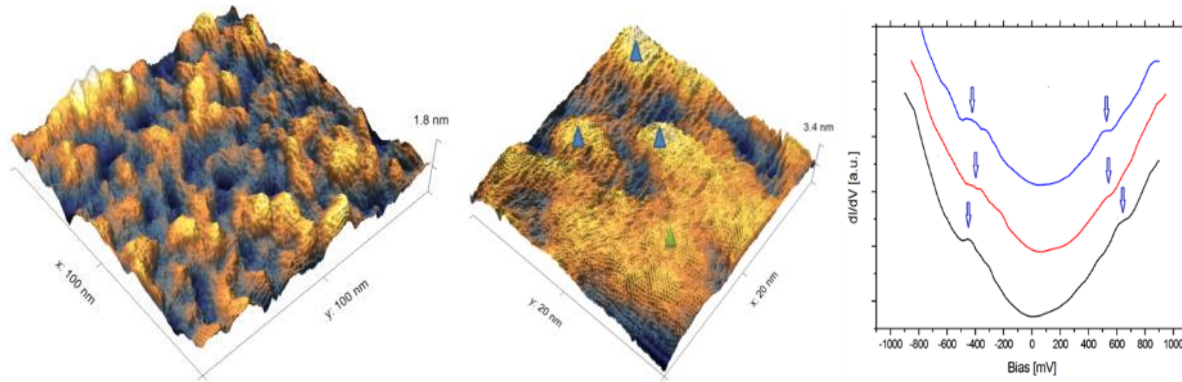
Fig. 8. *STM images of ultra-corrugated graphene sheets on SiO_2/Si substrate. Tunneling spectroscopy data reveals that electrons can be efficiently confined within the nanoscale corrugations.*

Our DFT calculations confirmed that pronounced charge localization occurs on the top of nanoscale graphene wrinkles. For such a graphene wrinkle, pseudo-Landau levels emerge in the electronic structure, corresponding to the equivalent of a 70 T magnetic field. This is due to the strain induced pseudo-magnetic field within the graphene wrinkles.
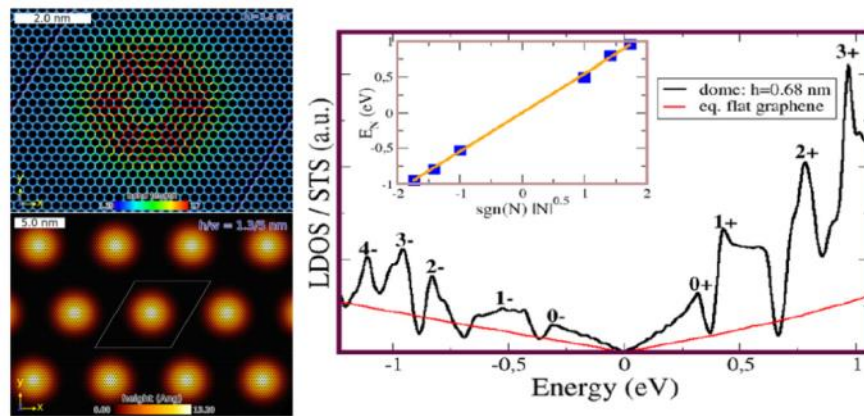
Fig. 9. *The atomic structure of a graphene corrugation and the corresponding pseudo-magnetic field (upper left), giving rise to Landau level like electronic states as evidenced in the calculated local density of states (right).*

Most importantly, Raman measurements on ultra-corrugated graphene sheets display a huge enhancement of the Raman signal of adsorbed molecules (Fig. 10).
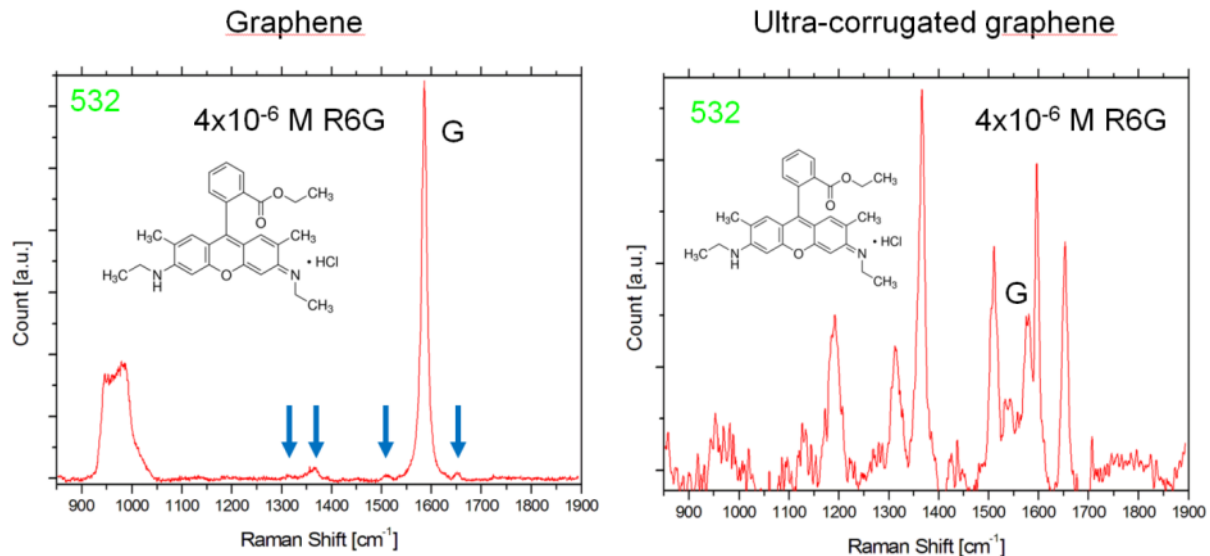
Fig. 10. *The Raman spextra of Rhodamin6G molecule detected from the same low concentration solution on flat and ultra-corrugated graphene substrates.*

The most likely explanation for the enhancement of the Raman signal of adsorbed molecules is that due to the confinement of the charge carriers within the nanoscale corrugation the electromagnetic mechanism of the surface enhanced Raman scattering is switched ON, through scaling the resonance frequency of graphene plasmons from THz region up to the visible through their nanometer scale lateral confinement. The presence of visible graphene plasmons have been confirmed by ellipsometry and electron energy loss spectroscopy (EELS) measurements.

Intra-valley charge carrier scattering on graphene corrugations

P. Kun, G. Kukucska, J. Koltai J. Kürti, L.P. Biró, L.Tapasztó, P. Nemes-Incze. Nature Commun. under review – preparing revised manuscript

The pseudo-magnetic field generated by mechanical strain (corrugations) in graphene can have dramatic consequences on the behavior of charge carriers. We have shown that the pseudo-magnetic field fluctuations present in crumpled graphene can induce significant intra-valley scattering of charge carriers. We have demonstrated that the charge carrier scattering on graphene corrugations can be detected by measuring the confocal Raman spectra of corrugated areas, where an increase of the D'/D peak intensity ratio by up to a factor of 300 can be observed. Scattering by point defects increases the intensity of D peak but not the D'. By contrast, inter-

valley charge carrier scattering by strain fluctuations increase the D' peak instead of the D peak. Thus the scattering by strain can be separated from other type of scattering by simple Raman spectroscopy measurements.
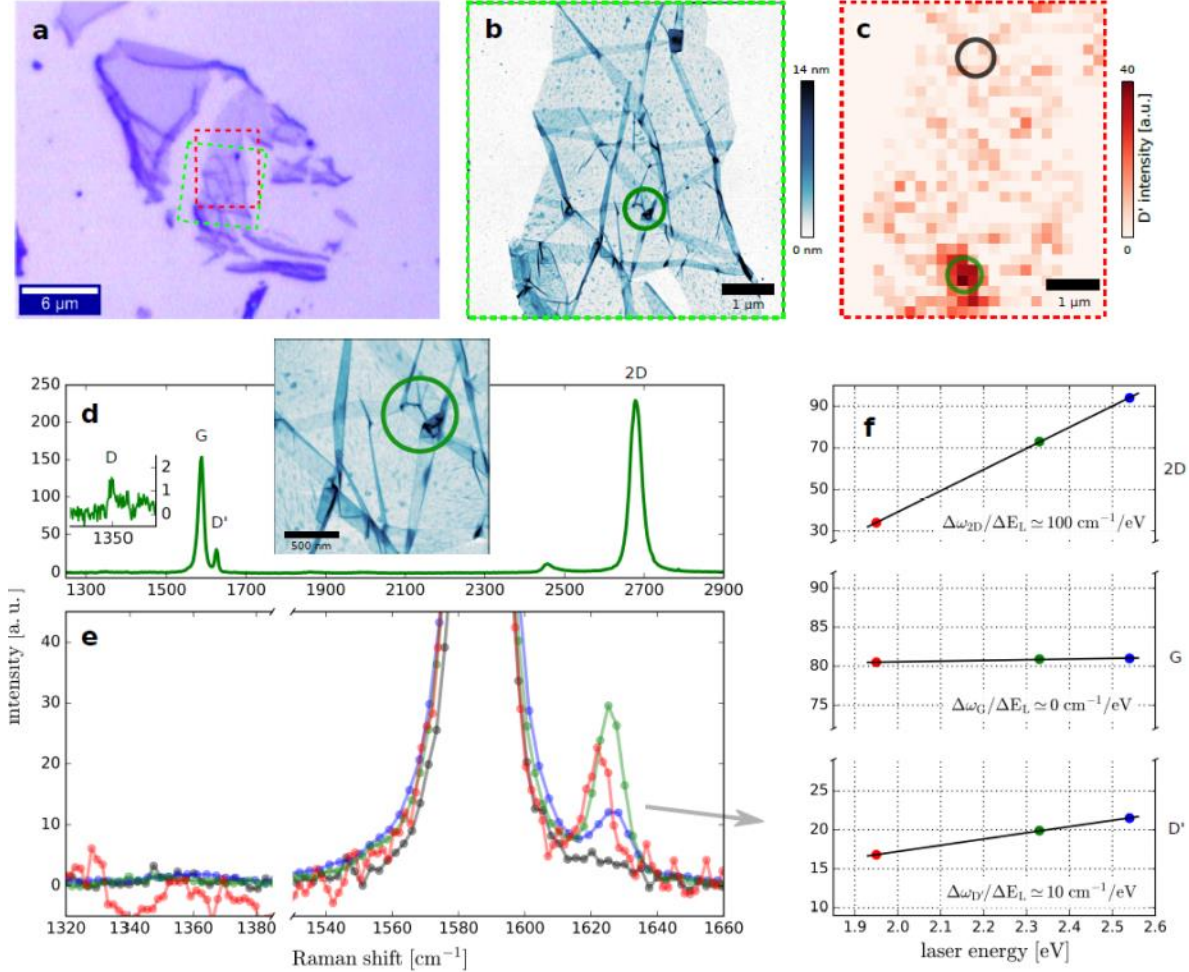
Fig. 11. *(a) Optical microscope image of an exfoliated graphene layer on SiO_2. (b) AFM image of crumpled area. Position within flake shown by green rectangle in (a). (c) Raman spectroscopy map of D' peak intensity of the crumpled graphene area. Map position within flake shown by red rectangle in (a). (d) Raman spectrum showing a large D' peak measured at the crumpled area shown in (b) and (c), inset: larger magnification AFM image of the crumpled area. Inset: zoom of the D peak region of the spectrum. (e) D' peak of the area shown in (d), measured with three different lasers. (f) change in the peak position of the 2D, G and D' peaks, as a function excitation energy, for the area marked by the red circle in (b, d).*

We were able to reproduce our experimental results by numerical calculation of the double resonant Raman spectra and interpret the results as experimental evidence of the phase shift suffered by Dirac charge carriers in the presence of a pseudo-magnetic field. This lifts the restriction on complete intra-valley backscattering of Dirac fermions.
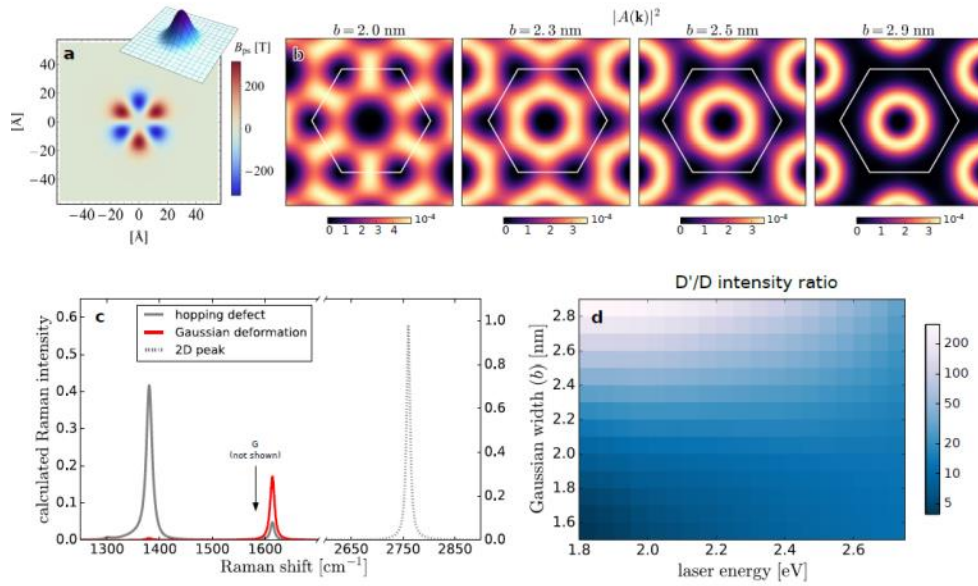
Fig. 12. *Calculated resonant Raman spectra. (a) Gaussian shape model used in Raman calculations. Color plot shows the calculated pseudo-magnetic field pattern for the deformation. (b) Plot of $|A(\mathbf{k})|^2$ in the first Brillouin zone (white hexagon). (c) Calculated D and D' peak intensity for a Gaussian deformation seen in (a). (d) Ratio of D' and D intensities (ID0/ID) as a function of excitation energy and Gaussian width.*

These results open up the way to the exploration of tailor made strain profiles in graphene and enable the design of new device concepts, using strain engineering.

Correlated electronic states in graphene

G.Z. Magda, X. Jin, I. Hagymási, P. Vancsó, P. Nemes-Incze, Z. Osváth, C. Hwang, L.P. Biró, L.Tapasztó.
Nature, 514, 608-611 (2014)

P. Vancsó, I. Hagymási, L. Tapasztó 2D Materials 4, 024008 (2017)

We proposed to investigate potential correlated electronic states in graphene emerging due to mechanical strain. The possibility that such states can emerge were based on the observation of a peculiar superlattice observed in the STM images of graphene grown on Cu 110 substrates. At that time only room temperature STM measurements have been available. The observed superlattice was apparently incommensurate with both the substrate and the graphene lattice, which pointed towards its electronic origin, such as an incommensurate charge density wave state. Theoretical attempts from our side to understand the emergence of such an electronic state in strained graphene have not been successful. Therefore to further clarify the observed phenomenon we have performed low temperature STM investigations.

The more precise low temperature measurements, free of image distortions due to the thermal drift found that in principle the observed superlattice is commensurate with the underlying Cu 110 surface, as a 6x2 superlattice reconstruction of the Cu 110 surface (Fig. 13).

In the view of the new experimental results it was more feasible to attribute the origin of the observed superlattice to the intercalation of the graphene / Cu (110) interface by oxygen. Oxygen is known to produce under certain concentrations a 6 x 2 reconstruction of the Cu 110 surface. This finding is very interesting on its own; however it is not related to the strain. As it was not fitting with the proposal of the present project we decided not to include these results in the present report.
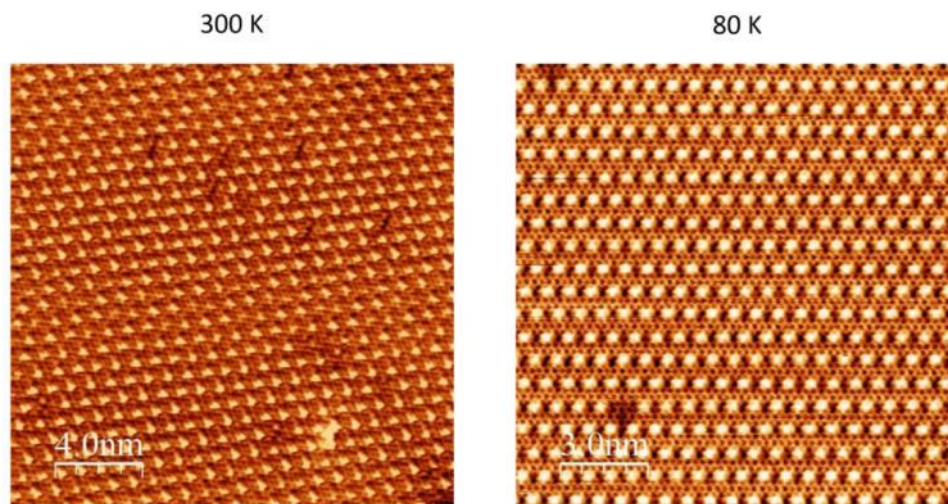
Fig. 13 *Atomic resolution STM images acquired at room temperature and at 80 K of graphene on Cu 110 displaying a peculiar rectangular superlattice that most likely can be attributed to the intercalation of oxygen resulting in a 6 x 2 reconstruction of the Cu 110 surface underneath the graphene.*

Nevertheless, we have studied correlated electronic states in graphene that emerge on graphene edges of a certain high symmetry direction (zigzag edges).

To realize graphene nanoribbons with precisely controlled crystallographic edge orientations, we employed a nanofabrication technique based on scanning tunneling microscopy. By acquiring atomic resolution images, the crystallographic directions of the graphene lattice can be identified and matched with the desired cutting directions. The direct cutting of graphene is done by chemical etching activated by the sub-nanometer wide channel of tunneling electrons, locally breaking the carbon-carbon bonds underneath the atomically sharp STM tip apex. Using the STM nanolithographic technique, we have defined nanoribbons into chemical vapor deposition grown graphene sheets deposited on gold substrates with large Au (111) terraces. Nanoribbons with pre-defined zigzag edge orientation and widths ranging down to 3 nm have been defined (Fig. 14).
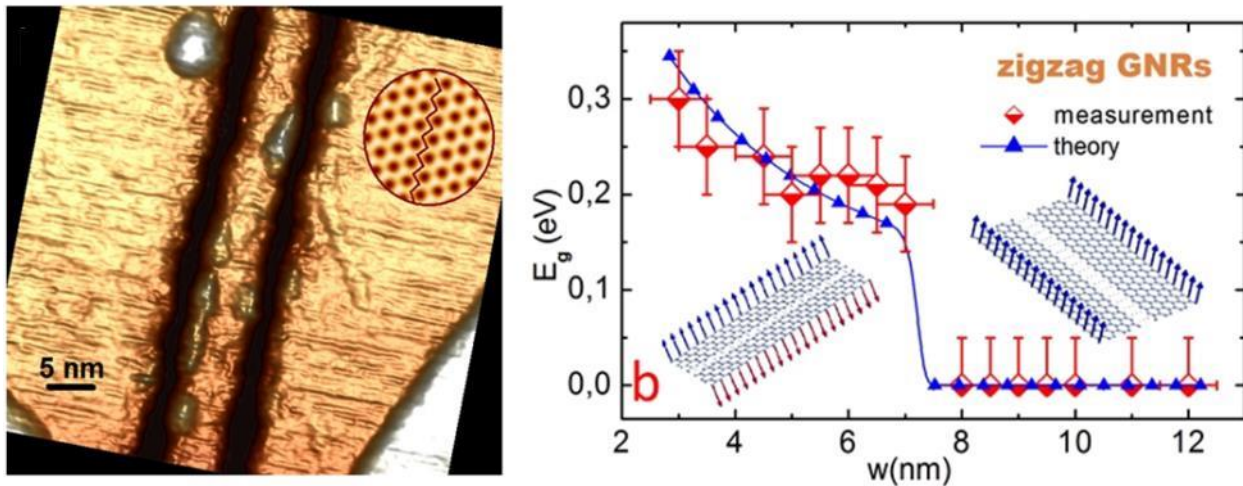
Fig.14. *Correlated electronic states on zigzag edges of graphene nanoribbons. a) STM image of a 6.5 nm wide graphene ribbon with edges of precisely zigzag orientation patterned by scanning tunneling lithography. b) The bandgap measured by tunneling spectroscopy as a function of ribbon width in zigzag ribbons. Theoretical data points have been calculated using the mean field Hubbard model.*

For zigzag ribbons narrower than 7 nm a fairly large bandgap of about 200 - 300 meV has been observed. The broadly predicted origin of bandgap opening in zigzag ribbons is electron-electron interactions and the predicted many-body ground state implies the magnetization of the edges. However, in contrast to first principles theoretical predictions in the literature, the measured gap suddenly vanishes for zigzag ribbons wider than 8 nm (Fig. 14). To understand the origin of the experimentally observed sharp semiconductor-metal transition, we have performed calculations based on the mean-field approximation of the Hubbard Hamiltonian that accounts for both finite temperature and doping. The main result of our extended theoretical model is that it reproduces the steep semiconductor-metal transition, quantitatively accounting for both the critical ribbon width (w ~ 7 nm) at which the transition occurs and the magnitude of the measured

bandgaps, using the strength of the on-site repulsion as the single unknown parameter. From calculating the spin density distribution for both semiconducting (w < 7 nm) and metallic (w > 8 nm) ribbons the origin of the observed semiconductor→metal transition can be identified as a transition from an antiferromagnetic (semiconducting) state, where magnetic moments on opposite ribbon edges are aligned antiparallel, to a ferromagnetic (metallic) state, with parallel spin alignment on opposite edges (Figure 15).
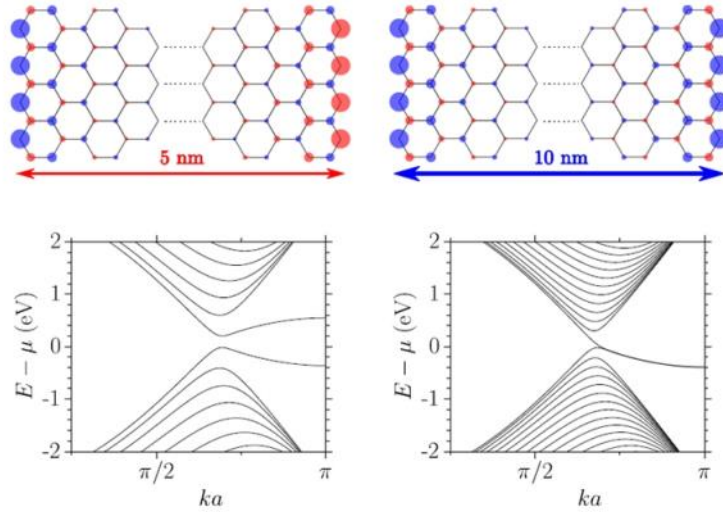
Fig.15. *Correlating electronic and magnetic properties of zigzag graphene nanoribbons. Spin density distribution ($\uparrow$ - blue, $\downarrow$ - red) in a 5 and 10 nm wide zigzag graphene nanoribbon calculated in the mean field Hubbard model for T = 300 K and $\Delta E_F \sim 100$ meV. Lower panels display the corresponding band strcuture, clearly indicating that narrow zigzag ribbons are antiferromagnetic semicondcutors, while wider (w > 8nm) zigzag ribbons display a ferromagnetic inter-edge coupling and no bandgap.*

However, even for narrow ribbons, slightly above the antiferromagnetic (AFM) ground state energy a ferromagnetic (FM) configuration exists with parallel spin orientation on both edges. In contrast to the half-filled system, where the AF state is always more stable, in a doped ZGNR, both AF and FM sates can become energetically favorable. Most importantly, there is an intriguing interconnection of the spin configuration and the electronic band structure that renders the ribbons in the AF spin configuration insulating, while FM nanoribbons are metallic. We have shown experimentally that a sharp transition from semiconducting (AF) to metallic (FM) state can indeed occur as a function of the ribbon width. However, varying the ribbon width is not a practical parameter for device applications. By using the same experimentally validated theoretical model, we show that the sharp semiconductor (AF)-metal (FM) transition can also be induced through changing the carrier density (n_{2D}) of the zigzag GNR. Our calculations, based on the Hubbard model and the Landauer transport formalism, reveal that the novel switching mechanism based on magnetic phase transition enables excellent field effect transistor (FET)

characteristics, and the device can also carry spin-polarized current. This is enabled by the fact that in contrast to the conventional FETs, where upon gating the electronic structure remains unchanged, only the charge density is modulated, in an correlated electron system the density of states depends strongly on the electron density. The main advantage of our device concept is that the carrier density in zigzag GNR can be easily tuned using a back gate electrode, therefore neither external magnetic field nor transverse electric field is required to control both the charge and spin currents in the device.
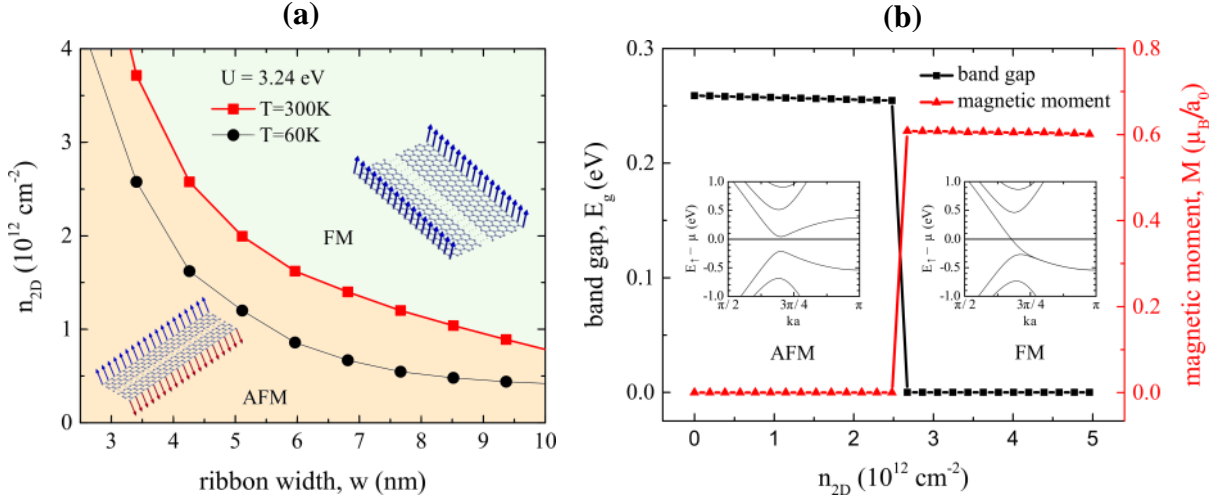
Fig. 16 *(a) Phase diagram of zigzag GNRs as a function of charge carrier concentration (n_{2D}) and ribbon width (w) at two different temperatures (T=60K and T=300K). (b) A sharp transition in the band gap and magnetic moment of a zigzag GNR (w=4.2 nm) occurs as a function of charge carrier density at room temperature.*

Figure 16 shows the phase diagram of zigzag GNRs as a function of ribbon width and charge carrier density, as calculated from the Hubbard Hamiltonian.

At T=0K (Figure 16a) below the phase transition carrier concentration the conductance is zero according to the presence of the band gap in the AFM configuration. Reaching the critical value of doping ($n_{2D}=1.6\times10^{12}$ cm^{-2}) the ZGNR becomes metallic (FM configuration) due to the open conduction channels for both up and down spins at the Fermi energy. The equal number of conduction channels for the different spin directions implies that the current is not spin polarized even though the ribbon itself is spin polarized ($n_\uparrow > n_\downarrow$). However, the current can become spin polarized by further increasing the charge carrier concentration (gate voltage) to $n_{2D}=8.7\times10^{12}$ cm^{-2} where additional conductance channels open for spin down while the number of conductance channel for spin up state remains the same. This asymmetry of the band structure for up and down spins in the FM configuration enables our device to carry spin polarized current. Consequently, our device layout does not require the use of an external magnetic field, ferromagnetic contacts or transvers electric fields to achieve spin polarized current, which is a huge technological advantage. Another intriguing property of our device is that the charge and

the spin currents can be independently tuned by the charge carrier density (sweeping the gate voltage).
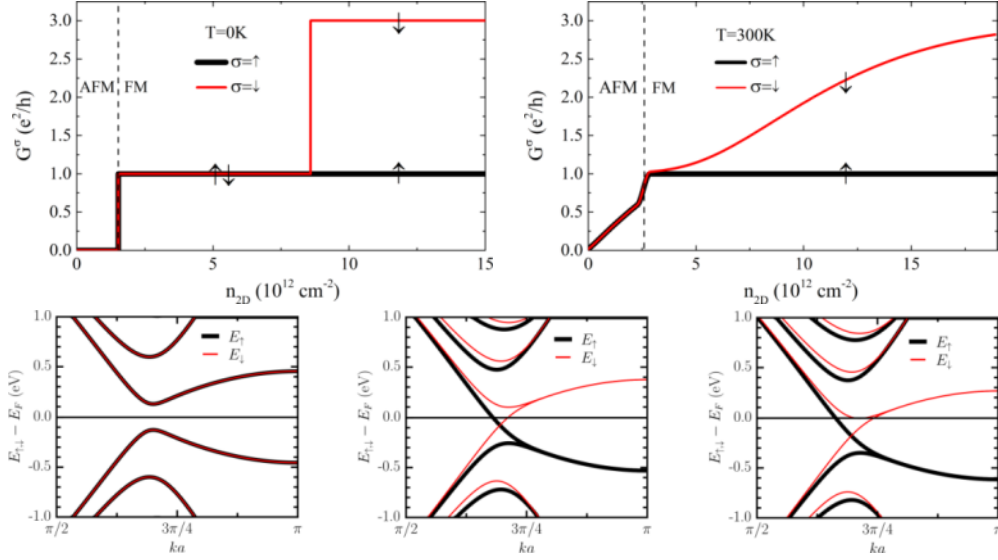
Fig. 17. *Spin dependent conductance as a function of charge carrier density for a 20-zigzag GNR at (a) T=0K and (b) T=300K. (c-e) Spin resolved band structure in the three operation regimes for: 0 cm⁻², 3×10¹² cm⁻², and 10¹³ cm⁻² at T=0K, respectively.*

The temperature has two important effects: (1) it shifts the position of the AFM-FM (semiconductor-metal) transition, and (2) it modifies the shape of the conductance plateaus due to the broadened energy distributions of the incident electrons described by the Fermi-function. In contrast to the step-like transition of both charge and spin current for the T=0 K case, at room temperature both transitions become gradual, due to combined effect of the temperature and doping. In contrast to the sharp switching of spin polarization form 0% to 50% at low temperatures (0K), at room temperature the spin polarization degree of the current can be continuously tuned between 0 and 50% by sweeping the back-gate voltage. This provides us a fully electrical control through a simple back gate electrode over the spin polarization degree of the current, which could be exploited in future spintronic devices. In principle, such a ribbon could act as spin source replacing ferromagnetic electrodes, which would be a huge technological advantage and on the long run enabling all-graphene spintronic circuits.

OFF

ON

$$I_{SD\uparrow} = I_{SD\downarrow} \neq 0$$

S   D

$$I_{SD\uparrow} = I_{SD\downarrow} = 0$$

S   D

$$V_G = 0.17\ V$$

$$V_G = 0\ V$$

$$I_{SD\downarrow} \sim 3\ I_{SD\uparrow} \neq 0$$

S   D

$$V_G = 0.4\ V$$
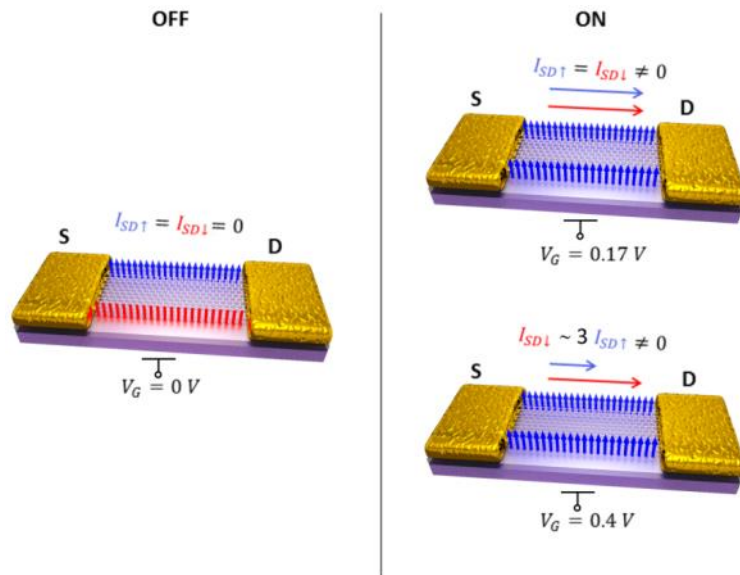
Fig. 18. *Schematic of a graphene nanoribbon field effect transistor with tunable spin polarization*

Strain engineering and superlattices in other 2D materials

Besides graphene, other two dimensional materials become more and more into the focus of the research efforts. While at the time of writing the proposal we were not yet aware of this trend, it became fairly obvious during the project. Therefore, to keep our research at the cutting edge of the field, we also extended our investigations originally planned for graphene to other 2D materials. The most widely investigated family of 2D crystals beyond graphene is the class of transition metal chalcogenides.

Fabricating single layer transition metal chalcogenides

G. Z. Magda, J Pető, G. Dobrik, C. Hwang, L. P. Biró, L. Tapasztó Scientific Reports, 5, 14714 (2015)

Isolating large-areas of atomically thin transition metal chalcogenide crystals is an important but challenging task. The mechanical exfoliation technique can provide single layers of the highest structural quality, enabling to study their pristine properties. However, a major drawback of the technique is the low yield and small (typically < 10 micron) lateral size of the produced single layers. Here, we report a novel mechanical exfoliation technique yielding MoS_2 single layers with typical lateral sizes of several hundreds of microns. The idea is to exploit the chemical affinity of the sulfur atoms that can bind more strongly to a gold surface than the neighboring layers of the bulk MoS_2 crystal. Moreover, we found that our exfoliation process is not specific to MoS_2, but can be generally applied for various layered chalcogenides including selenides and tellurides, providing an easy access to large-area 2D crystals for the whole class of transition metal chalcogenides.

Graphene displays an ultra-strong adhesion to SiO_2, which plays an important role during the exfoliation process, facilitating the exfoliation of large (typically tens of microns) single layers. To improve the exfoliation process of MoS_2 single layers we propose to improve their adhesion to the substrate. To achieve this, instead of the usually employed SiO_2/Si, we used gold substrates exploiting the chemical affinity of the sulfur to gold to achieve a stronger adhesion.

In optical microscopy images the exfoliated MoS_2 single layers on top of gold can be identified as the areas of the faintest color contrast as shown in Fig. 19. The optical images revealed several hundreds of microns large areas covered by atomically thin MoS_2 layers. To confirm that these areas of faintest optical contrast are indeed single layers of MoS_2 we have performed confocal Raman spectroscopy measurements as shown in the inset of Fig.19b. We have observed the characteristic MoS_2 peaks (E_{2g}, A_{1g}) around 384 and 404 cm^{-1}, wavenumbers respectively. This indicates that the several hundreds of microns large areas detected by optical microscopy can be identified as MoS_2 single layers.
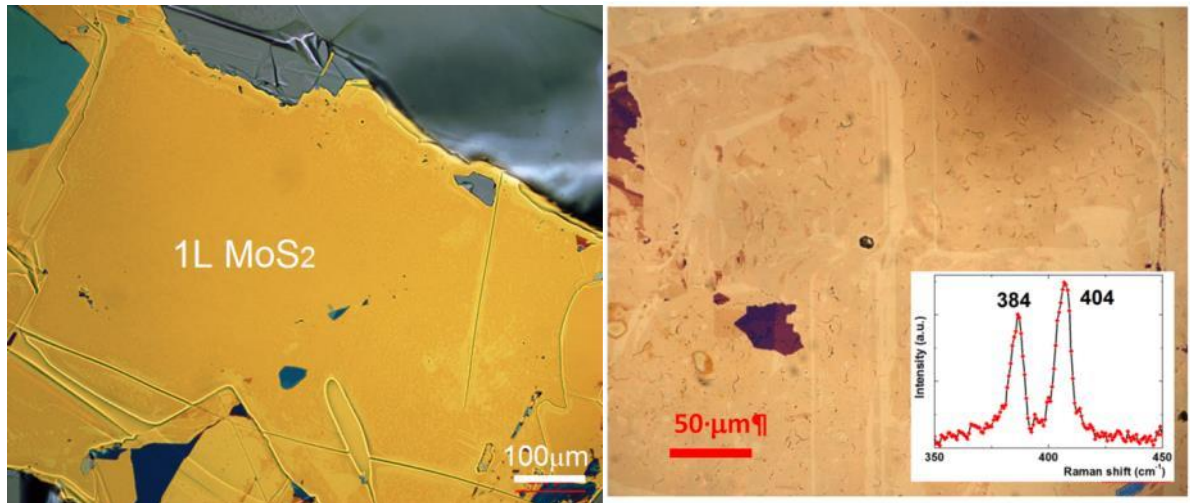
Fig. 19 *Optical microscopy images of MoS₂ single layers with several hundreds of microns lateral size exfoliated on gold (Au) substrate. The large areas of the faintest optical contrast have been confirmed to be single layers by Raman spectroscopy (inset).*

We have also investigated whether the exfoliation process is specific to MoS$_2$ or can be applied more generally to various layered materials. We found that our exfoliation method yielding large-area MoS$_2$ flakes is not specific to molybdenum disulfide or even sulfides, but works equally well for various layered chalcogenides, including selenides and tellurides.

The atomic scale defect structure of MoS$_2$ single layers

P. Vancsó, G. Z. Magda, J. Pető, J Noh, Y. Kim, C. Hwang, L.P. Biró, L. Tapasztó
Scientific Reports 6, 29726 (2016)

Transition metal chalcogenide single layers have emerged as strong competitors of graphene in electronic and optoelectronic applications. However, electrical transport and photoluminescence measurements indicated the presence of a high concentration of point defects substantially altering their intrinsic electronic and optical behavior. Here, we report the STM observation of a high density of structural point defects in MoS$_2$ single layers, which have been identified as sulfur atom vacancies. Besides resolving the atomic structure of the MoS$_2$ defects, we were also able to identify the electronic midgap states induced by the presence of point defects, by combining STM measurements with *ab intio* calculations.

Atomic resolution imaging of the MoS$_2$ single layers can be achieved even under ambient conditions. Although imaging the hexagonal lattice of the top layer of sulfur atoms can be routinely achieved, resolving individual point defects was only possible for the very best imaging and tip conditions. These images clearly revealed the atomic scale structural defects of the MoS$_2$ single layers (see Fig.20). Even after long scanning times the number of defects and their spatial distribution remained unchanged in the scanning area, evidencing the noninvasive nature of the STM measurements.
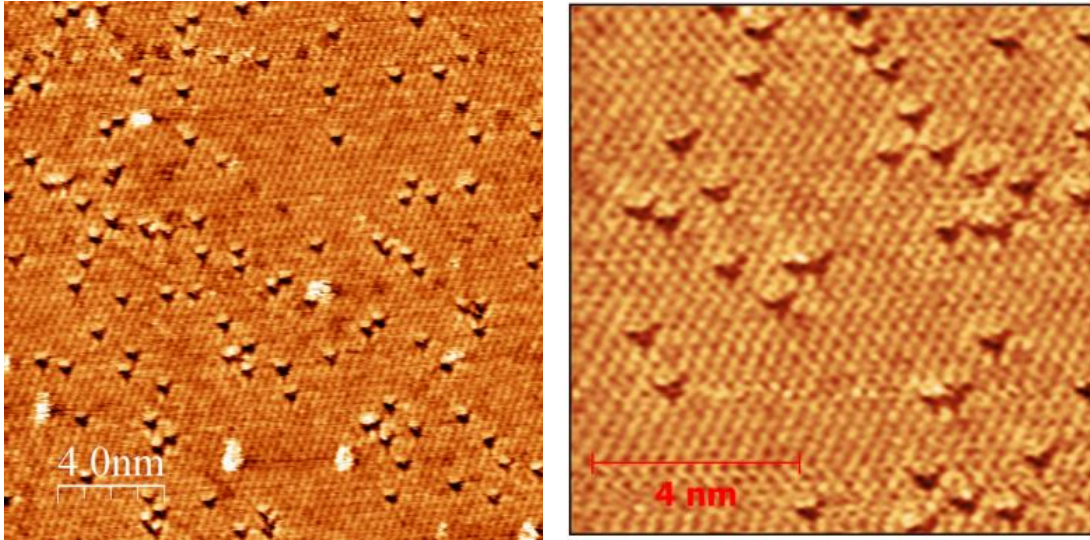
Fig. 20 *Atomic resolution STM images of exfoliated MoS$_2$ single layers on Au 111. The dark triangular features can be identified as single sulfur atom vacancies.*

Fig. 20 shows atomic resolution STM images of a MoS$_2$ single-layer. The main feature observed is a hexagonal lattice of 0.31 nm periodicity, corresponding to the atomic lattice of the top sulfur layer of the 2D MoS$_2$ crystal. By contrast, dark triangles are atomic scale discontinuities stable both in number and position during long scanning times. Line profiles across the dark triangles reveal that they are centered on the position of a missing S atom, indicating their S vacancy origin. Since during the STM investigation the introduction of novel point defects has never been observed, we can directly estimate their intrinsic concentration in high quality exfoliated MoS$_2$ single layers. Based on several STM images we found that the distribution of the point defects is non-uniform across the sample surface, with their native concentration typically ranging from 5×10^{12} to 10^{13} cm^{-2} values.

We were also able to study the electronic properties of point defects in single-layer MoS$_2$, by comparing atomic resolution STM topography data on defects with *ab initio* density functional (DFT) calculations. Using DFT calculations sulfur vacancies (V$_S$'s) were identified as observed point defects. In addition, we were able to identify the signature of two defect induced midgap states of a single sulfur atom vacancy in the band structure of MoS$_2$ single layer.
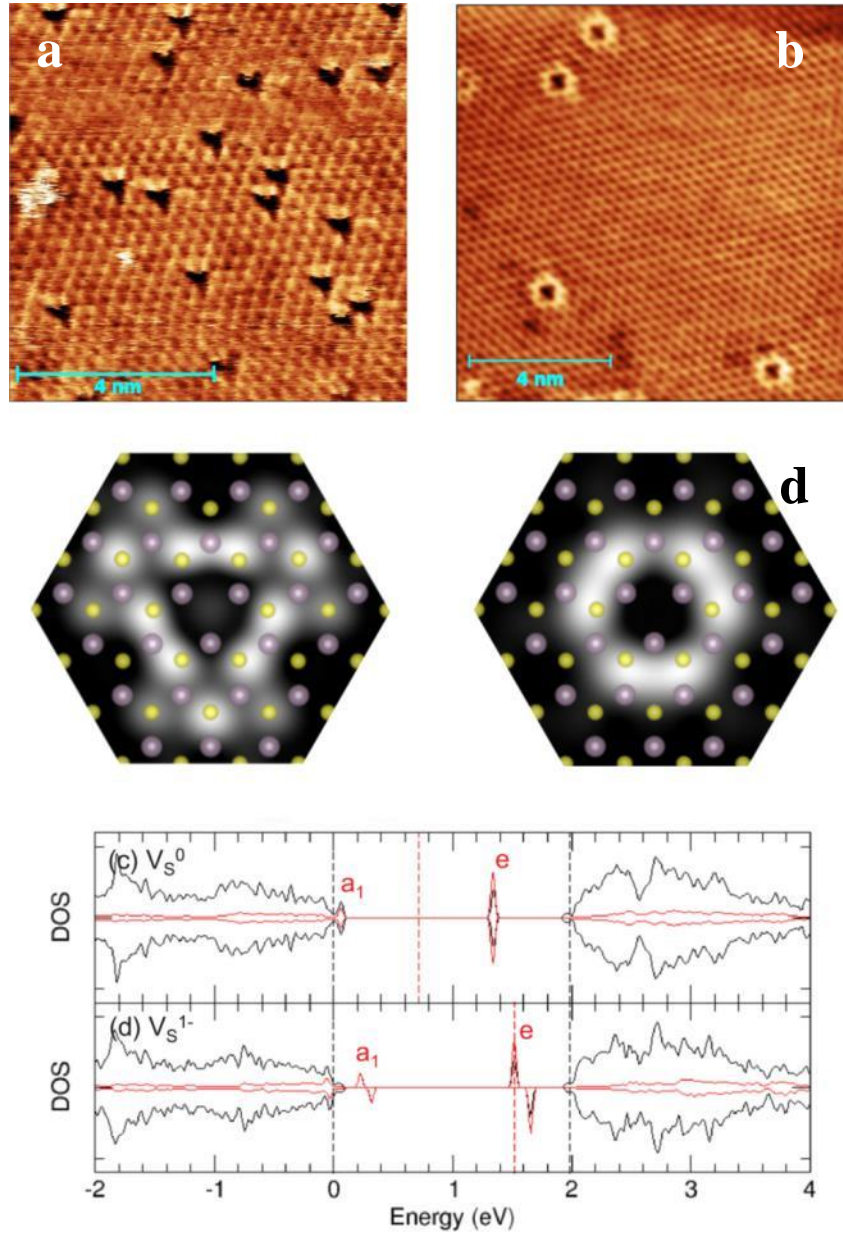
Fig. 21. *(a,b) Atomic resolution STM images of single-layer MoS$_2$ with triangular and circular shaped point defects, and the corresponding simulated STM images of the neutral sulfur vacancy (V_s^0) a$_1$ and e states (see image c) based on the DFT calculations. The sulfur and molybdenum atoms are shown by yellow and purple circles, respectively. (c,d) Density-of-states for V_s^0 and V_s^{1-} where the a$_1$ and e defects states in the band gap are marked.*

Fig. 21 show the simulated STM images from the calculated local density of states of the neutral *a$_1$* and *e* states, respectively. The localization of the electronic states within 5Å radius surrounding the removed S atom can be clearly seen, where the *a$_1$* state has a triangular form, while the doublet *e* states have an apparent circular symmetry in excellent agreement with our STM measurements. Consequently we propose that the two high contrast defect states observed

experimentally can both be attributed to different localized electronic states of the same S vacancy defect.

2D MoS₂ superlattice on graphite substrate

A.A Koós, P. Vancsó, G.Z. Magda, Z. Osváth, K. Kertész, G. Dobrik, C. Hwang, L. Tapasztó, L.P Biró
Carbon, 105, 408 (2016)

MoS₂ single layers were produced by atmospheric pressure chemical vapor deposition (CVD) in a two zone tube furnace heated to 190 and 650 °C, respectively. The furnaces were heated to and cooled from growth temperature without precursors; they were moved into growth position at the beginning of the growth cycle and moved away at the end. Therefore the temperature of the precursors changed significantly in a few seconds and we could reduce the effect of transition periods.
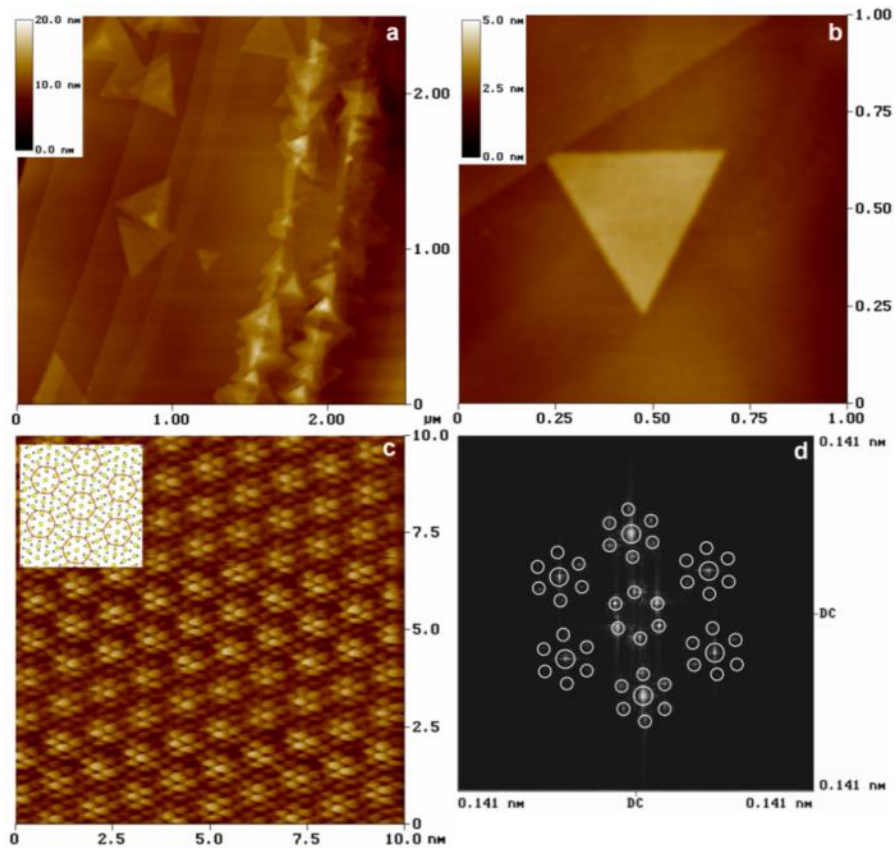
Fig. 22. *a) STM image of a MoS₂ flakes grown on graphite. b) Single layer MoS₂. c) Atomic resolution STM image of the MoS₂ monolayer displaying a moiré superlattice. The inset shows a ball and stick model of sulphur (yellow) and carbon (grey) atoms. The red circles denote the overlapping regions according to 4 – 5 periodicities of atomic distances. d) FFT of the atomic resolution image with highlighted spots.*

The MoS₂ flakes grow in a triangular shape and follow the crystallographic orientation of HOPG substrate. The nucleation had higher probability at graphite step edges than at defect free

areas; therefore the MoS_2 coverage became inhomogeneous (Fig. 22a). A typical triangular single layer flake is shown on figure 22b

The high resolution STM image (Figure 22c) shows two overlapped periodic structures which form a moiré superlattice. The smaller 3.15 Å period corresponds to the inter-atomic spacing of S atoms in MoS_2, while the longer 12.5 Å period is due to the interaction between MoS_2 and graphite. The moiré superlattice is also clearly visible in the Fourier transformed STM image (Figure 22d).. The 12.5 Å period is nearly 5 times the atomic distance in HOPG, and 4 times in MoS_2, respectively. The edges of the virtual hexagons on FFT image were almost parallel, except small deviations (of approximately 5°) between the crystallographic orientation of the MoS_2 and HOPG indicating a closely epitaxial growth.

MoS_2 superlattice on Au (111)

manuscript under preparation

Two types of moire superlattices have been identified in 2D MoS_2 on Au(111) by STM. The corresponding rotationally misoriented phases have been reproduced by density functional theory (DFT)-adaptive classical molecular dynamics (CMD) simulations and by DFT methods. In particular, the topography and morphology of the moire superlattices have been characterized in detail. The smaller phase, which has not been reported so far, with 1.1 nm periodicity exhibits a nanomesh (concave) morphology.
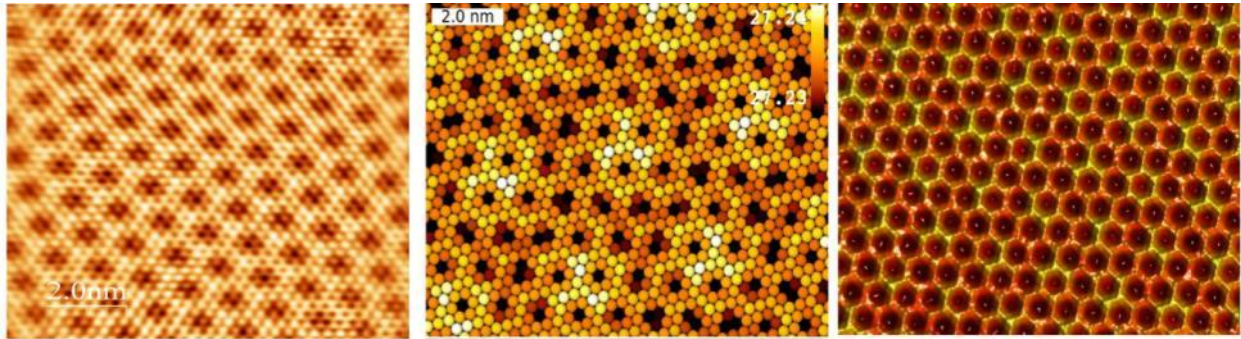
Fig. 23 *Atomic resolution STM measurement (left) of a MoS_2 single layer on Au(111) substrate revealing a nanomesh type (concave) superlattice geometry of 1.1 nm periodicity. Classical Molecular Dynamics (middle) and DFT simulations of the same system*

Ab initio DFT and molecular dynamics calculations at 5 and 300 K provide stable nanomesh morphology for the 1.1 nm phase using an accurate plane-wave algorithm. Various other rotated phases have also been predicted by CMD simulations.

Besides observing for the first time a nanomesh (concave) type superlattice in MoS_2 single layers, we have also observed the conventional convex superlattice of 3.2 nm periodicity.
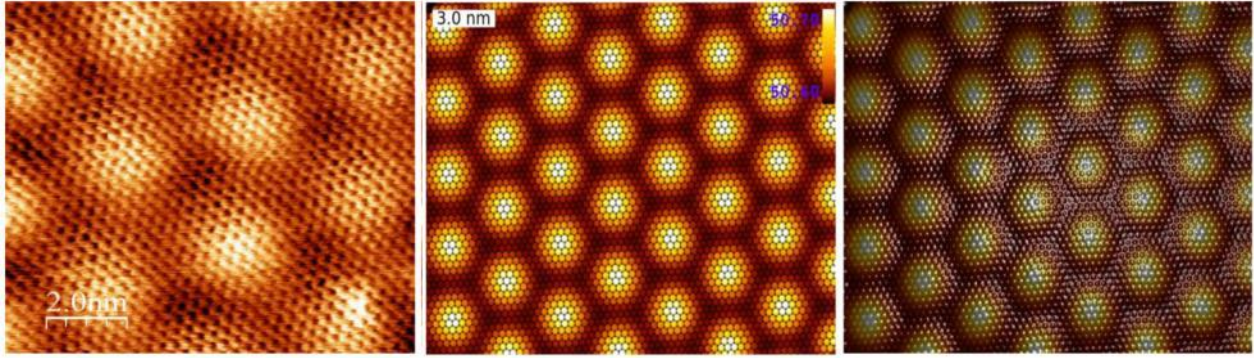
Fig. 24 *Atomic resolution STM measurement (left) of a MoS$_2$ single layer on Au(111) substrate revealing a convex superlattice geometry of 3.2 nm periodicity. Classical Molecular Dynamics (middle) and DFT simulations of the same system*

The periodic superlattice modulation of the atomic structure of the MoS$_2$ single layers is expected to influence the electronic properties of such 2D crystals. This will be the subject of further investigations.

Strain engineering of 2D MoS$_2$ crystals

manuscript under preparation

Most transition metal dichalcogenide crystals possess an intrinsic, direct band gap in the single layer limit. Owing to this, these materials could be particularly useful for nanoelectronic and opto-electronic applications. However, to exploit this potential we need the ability to tune their properties according to the requirements of the specific applications. Using mechanical strain to engineer the band gap of 2D MoS$_2$ crystals is a promising approach to this end. DFT calculations predict the band gap of 2D MoS$_2$ to decrease by approximately 0.2 eV for 1% strain introduced to the system. However, photoluminescence (PL) experiments conducted so far, could only provide data on the alteration of the direct band gap, which was found to be of about 0,1 eV for 1% of strain. We have performed scanning tunneling microscopy and spectroscopy investigations of nanobubbles in 2D MoS2 crystal on Au (111) substrate. Raman spectra on bubbles indicate that a biaxial strain of approximately 2-3 % exists within these bubbles. Our tunneling spectroscopy measurements revealed a band gap reduced to 1.1 eV on bubbles as compared to the original 1.8 eV gap. The much larger change of the band gap observed in our tunneling spectra, as compared to photoluminescence (PL) measurements, is due to the direct-indirect transition of the band gap induced by mechanical strain as predicted by DFT calculations. While PL only measures the change of the direct (optical) gap, our tunneling spectra provide the first experimental values for the strain engineering of the indirect (fundamental) gap, relevant for electronic applications.
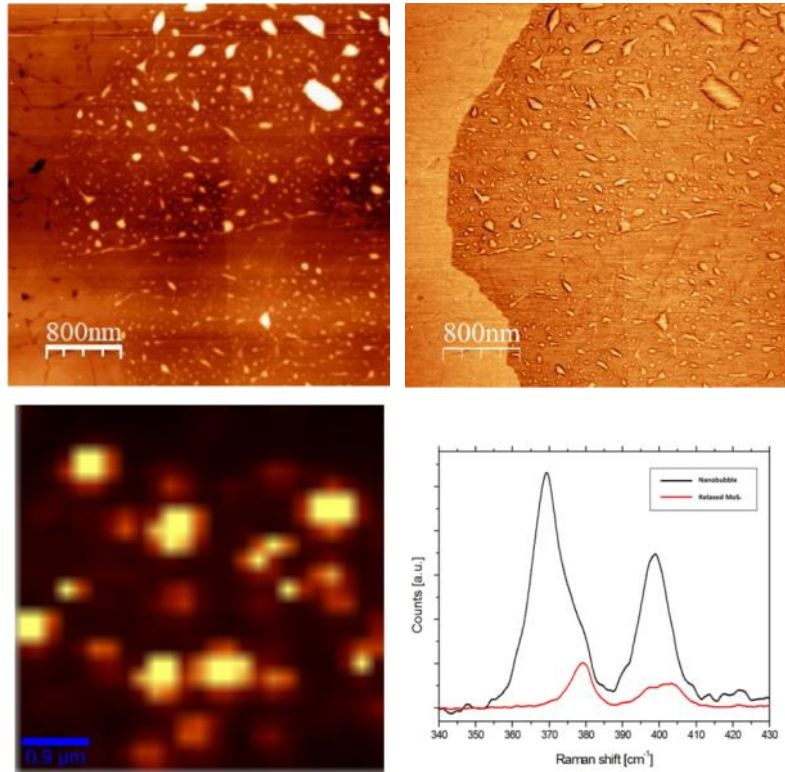
Fig. 25 *Atomic force microscopy image of MoS$_2$ monolayer on Au 111 displaying a high concentration of nanoscale bubbles.. Raman spectroscopy maps reveal that on such bubbles the MoS$_2$ lattice is substantially strained.*

The high density of nanobubbles revealed by AFM and STM investigations is prevalent. A typical nanobubble is characterized by tens of nanometer lateral size and a coupe of nm height. Nanobubbles form at the MoS$_2$/Au(111) emerge because the strong interaction between the MoS$_2$ and the Au is trying to maximize the overall attractive van der Waals interaction by squeezing the interlayer contamination into nanobubbles and establishing an atomically clean direct contact between the MoS$_2$ and Au 111 in all other areas.

In order to test the theoretically predicted significant band gap decrease upon strain we performed tunneling spectroscopy measurements on the nanobubbles where the deformation of the lattice is significant.
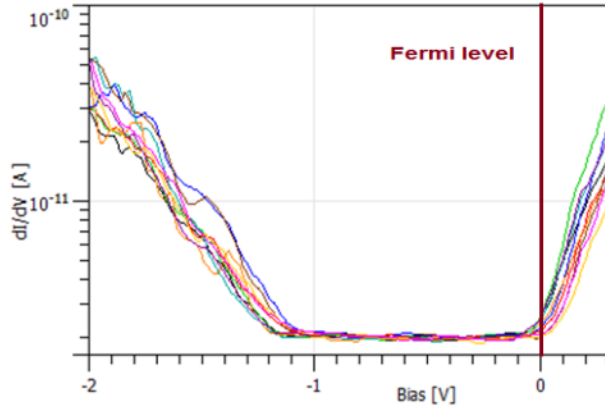
Fig. 26 Tunneling spectra at the center of a nanobubble displaying a band gap is only 1.1 eV, and the Fermi level shifted out of the gap into the edge of the conduction band.

While the intrinsic bandgap of the strain-free MoS_2 monolayer is about 1.8 eV, the nanobubble shows only a 1.1 eV wide band gap. Thus the band gap is decreased due to strain by about 0.7 eV. Our experimental findings clearly evidence that strain engineering is a very powerful tool for engineering the band bag op transition metal dichalcogenides.